Acta Geochim
https://doi.org/10.1007/s11631-024-00726-x

ORIGINAL ARTICLE

Ore-forming mechanism of Huxu Au-dominated polymetallic deposit in the Dongxiang Basin, South China: Constraints from *in-situ* trace elements and S–Pb isotopes of pyrite

Hongze Gao[1,2,3] · Jiajie Chen[1,2,3] · Chengbiao Leng[1,2,3] · Yuhui Hu[3] · Huidan Xie[3] · Zenghua Li[1,3]

Received: 15 May 2024 / Revised: 24 July 2024 / Accepted: 25 July 2024

Abstract The Huxu Au-dominated polymetallic deposit is a hydrothermal deposit located in the Dongxiang volcanic basin in the middle section of the Gan-Hang tectonic belt in South China. The orebodies primarily occur within the Jurassic-Cretaceous quartz diorite porphyry, while the genesis of this deposit is unclear. This study focused on geological and mineralogical characteristics, *in-situ* trace elements and S-Pb isotopes of three generations of pyrite of the Huxu deposit to clarify the distribution of trace elements in pyrite, ore-forming fluid and material sources, and genetic types of the deposit. The mineralization stage of the deposit can be divided into quartz-pyrite stage (S1), quartz-pyrite-hematite stage (S2), quartz-polymetallic sulfide stage (S3) and quartz-hematite stage (S4), with the corresponding pyrite being divided into three generations (Py1–Py3). *in-situ* trace element data of pyrite show that Au in pyrite mainly exists in the form of solid solution (Au^{+}), and the content is relatively low at all stages (0.18 ppm for Py1, 0.32 ppm for Py2, 0.68 ppm for Py3), while Pb and Zn mainly exist as sulfide inclusions in the pyrite. S-Pb isotopes show that the sulfur and ore-forming material of this deposit are mainly sourced from magma. The mineral association, mineral textures and trace elements in different stages of pyrite indicate that fluid boiling and fluid mixing are the key factors of native gold precipitation in S2 and S4, respectively, while water-rock interaction controlled the precipitation of Pb-Zn sulfides. These integrating with geological characteristics suggests that the deposit should be an intermediate sulfidation epithermal deposit.

Keywords Au-dominated · Polymetallic deposit · Intermediate sulfidation · Epithermal deposit · Pyrite · Trace element · S-Pb isotope · Tectonic belt

1 Introduction

Epithermal gold deposits are among the most important in the world, and > 6000 tons of gold resources 2018from epithermal systems have been proven (Zhong et al. 2017). They are widely distributed globally and also provide substantial amounts of silver, and some lead and zinc, holding significant economic value and research importance (Song et al. 2018). These deposits typically form at depths < 1.5 km, temperatures between 150 and 320 °C and pressures between 10 and 50 MPa. Epithermal deposits are categorized into three types: high sulfidation (HS), intermediate sulfidation (IS) and low sulfidation (LS) epithermal deposits. Compared to the other two types, research on intermediate sulfidation epithermal deposits is still relatively scarce, and the ore-forming mechanism of this type of deposit remains controversial (Yilmaz et al. 2010; Mehrabi and Siani 2012; Kouhestani et al. 2015; Song et al. 2018).

The Huxu Au-dominated polymetallic deposit is located in the middle section of the Gan-Hang tectonic belt (GHTB), where Jurassic-Cretaceous igneous rocks are widespread

Supplementary Information The online version contains supplementary material available at https://doi.org/10.1007/s11631-024-00726-x.

✉ Jiajie Chen
chenjiajie03@126.com

1 State Key Laboratory of Nuclear Resources and Environment, East China University of Technology, Nanchang 330013, China

2 National Key Laboratory of Prospecting, Mining and Remote Sense Detecting on Uranium Resources, Nanchang 330013, China

3 School of Earth Sciences, East China University of Technology, Nanchang 330013, China

Published online: 15 August 2024

(Fig. 1a). Many large to super-large porphyry or epithermal deposits have been uncovered in the eastern area of the GHTB, such as the Dexing porphyry Cu-Mo-Au deposits and the Yinshan epithermal Ag-Pb-Zn-Cu deposit, with most dating back to the Jurassic period (Mao et al. 2021). However, in the middle section of the GHTB, only a few medium-small hydrothermal deposits or occurrences have been uncovered in the Jurassic-Cretaceous volcanic basins. Among these basins, the Dongxiang volcanic basin, as a typical example, has several hydrothermal polymetallic deposits, including the Dongxiang copper deposit in the north (Cai et al. 2011, 2016; Ouyang 2015) and the Au-dominated polymetallic deposit (Au-Pb-Zn) (Liu et al. 1995; Wang et al. 1998), Huxingshan and Yinjianfeng gold deposits in the central part. At present, less attention has been paid to these medium-small hydrothermal deposits or occurrences. The genesis of these deposits, the difference in the mineralization processes between these deposits and the large deposits in the eastern area of the GHTB and whether there is potential for large hydrothermal deposits in this area are still unclear.

In this contribution, we focus on the Huxu gold polymetallic deposit in the Dongxiang volcanic basin. Detailed geological and petrography-mineralogy studies and *in-situ* trace element and S-Pb isotope analysis of sulfide have been carried out on this deposit to better understand mineralization process of the Huxu Au-dominated polymetallic deposit. The genetic type of this deposit is also discussed. The conclusions will provide insight to the regional metallogeny and the deployment strategies of prospecting work.

2 Regional geology

The GHTB is a significant polymetallic metallogenic belt in South China. It is also a collision suture zone between the Yangtze and Cathaysian Blocks, formed in the Late Proterozoic (Li et al. 2004; Sun et al. 2008; Mao et al. 2011). Since then, although the regional Caledonian and Indosinian orogenies have occurred, the GHTB has not been activated significantly as evidenced by the scarcity of the related magmatic rocks (Li and Li 2007). During the Jurassic-Cretaceous, due to the subduction and/or retreat of the Pacific plate, magmatic activities prevailed in the GHTB and thus resulted in the widespread volcanic and subvolcanic rocks in this area. This intense tectonic-magmatic event facilitated polymetallic mineralization, resulting in the formation of numerous hydrothermal metal deposits in the GHTB and adjacent areas (Mao et al. 2011; Hu et al. 2016).

The Dongxiang volcanic basin is one of the many volcanic basins in the middle section of GHTB. The basement of this basin is the Middle Proterozoic Shuangqiaoshan Group, and it is mainly composed of quartzite, mica schist, phyllite, metasiltstone, glutenite and sedimentary tuff. The main covers are Jurassic-Cretaceous rocks, including dominant medium-acid volcanic rocks (dacite, andesite) and pyroclastic rocks (tuff, agglomerate, etc.) of multiple eruptive cycles and secondary terrigenous clastic sedimentary rocks in the northwestern part of the basin (Fig. 1b). Minor coeval intrusive rocks are present in the basin, predominantly composed of intermediate acid subvolcanic intrusive rocks, such as diorite, dacite and andesite porphyry. These Late Jurassic to Early Cretaceous igneous rocks were dated at 149–124 Ma (Yang 2015), coeval with the igneous rocks in the adjacent Xiangshan (Yang et al. 2011), Shengyuan, Huanggangshan (Qin 2014) and Tianhuashan volcanic basins (Su et al. 2013). Most of these rocks are believed to have formed in an extensional environment caused by the retreat of Pacific subduction plates during the Late Jurassic to Early Cretaceous (Shu et al. 2017). The main structures in the Dongxiang volcanic basin include faults, folds and volcano-related structures, with fault structures being the most developed. Most of the faults are intruded by subvolcanic rocks and exhibit partial alteration, serving as the primary rock- and ore-controlling structures in the region (Wang et al. 1998; Yan et al. 2012a, b; Yang 2015).

3 Ore deposit geology

The Huxu Au-dominated polymetallic deposit is located in the north of the Dongxiang volcanic basin (Fig. 1b). The strata in this deposit are mainly the Late Cretaceous Hekou Formation and Early Cretaceous Daguding Formation (Fig. 1c). The Hekou Formation is mainly composed of red sandstone, calcareous sandstone and sandy conglomerate, primarily distributed in the northwestern part of the mining area. The Daguding Formation is mainly composed of rhyolitic and dacitic ignimbrite and a small amount of andesite. According to the lithology of the formation, the Daguding Formation can be divided into upper and lower sections. The lower section is dominated by stratified dacite, which is mainly distributed in the central and southern part of the mining area, while the upper section is dominated by tuffaceous mudstone, siltstone and sandstone, primarily distributed in the northern part of the mining area. The intrusive rocks in the mining area are mainly the late Yanshanian quartz diorite porphyry, distributed in the southeast of the mining area. This quartz diorite porphyry, spatially constrained by volcanic structure and influenced by the F13 fault in the northwest area of the mining area, exhibits wavy-like contacts with other strata (Fig. 1c) (Wang et al. 1998; Yan et al. 2012a, b; Wan et al. 2020). The faults in the mining area are prevailing, and there are divided into two groups, namely NE- and NW-trending faults. The NW-trending fault (F13 fault, Fig. 1c) in the north of the mining area is characterized by filled fracturing rocks and shows characteristics of

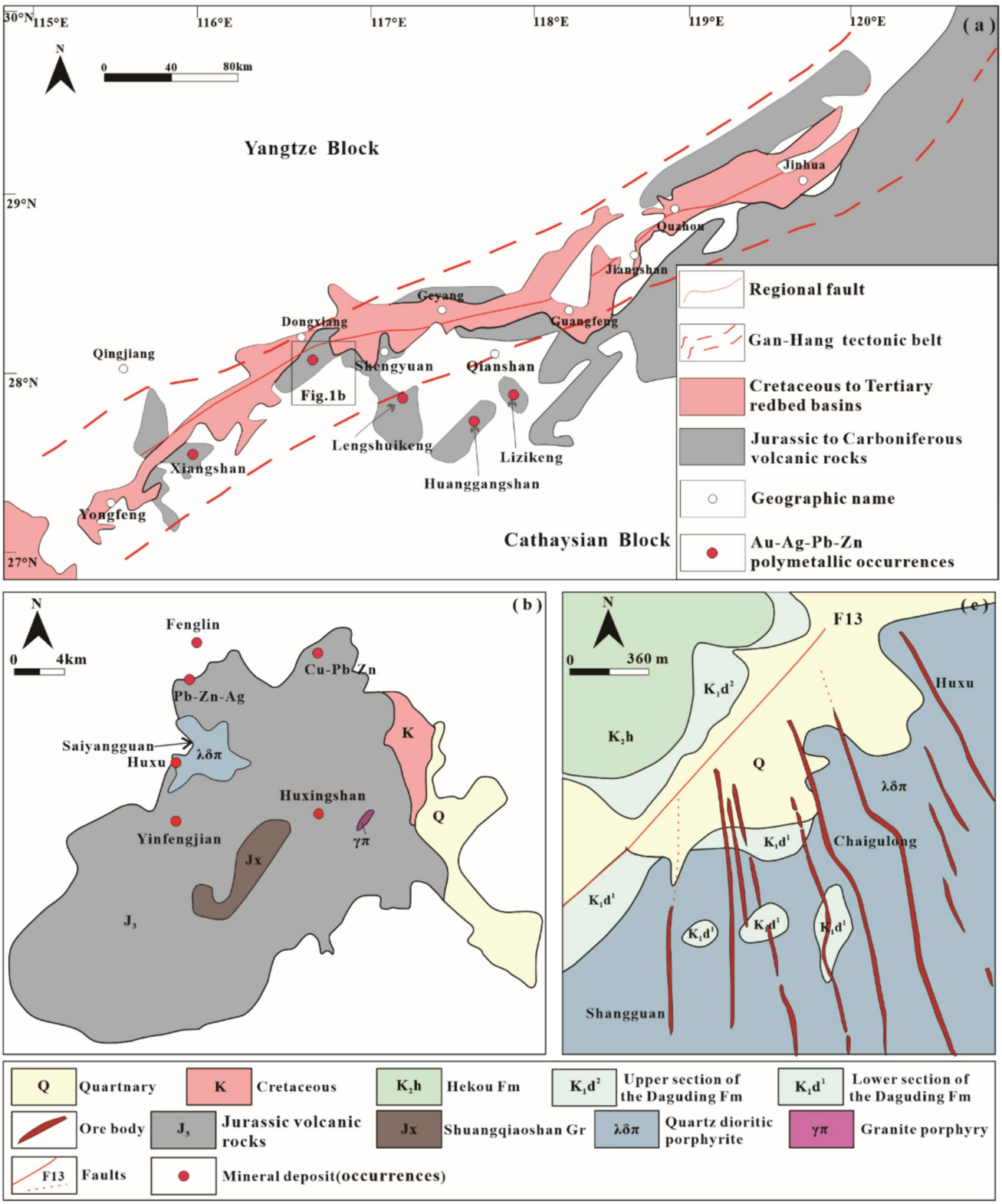

Fig. 1 **a** Sketch geological map of the Gan-Hang tectonic belt (modified after Yu et al. 2006); **b** geological map of the Dongxiang volcanic basin (modified after Yan et al. 2012a, b); **c** geological map of the Huxu Au-dominated polymetallic deposit (modified after Zhou et al. 2019)

multiple activities (Wang et al. 1998). Several NW-trending faults are located to the southeast side of F13 and are the main ore-bearing faults.

The Huxu Au-dominated polymetallic deposit is composed of three ore blocks, namely, Huxu, Chaigulong and Shangguan (Fig. 1c). The ore bodies primarily occurred in the southwest of the Saiyangguan quartz diorite porphyry and locally in the volcanic clastic rocks (Fig. 1c). The ore in the mining area is mainly divided into two types: quartz-sulfide type and quartz-hematite type. The gold in the quartz-sulfide type is mainly in the form of invisible gold, with minor amounts in the form of visible gold, while in the quartz-hematite type ore, it is mainly in the form of visible gold (Wang et al. 1998) and primarily exists in the quartz fissure and its interior. Massive, vein-like, miarolitic, breccia and druse-like ores can be observed in the Huxu deposit (Fig. 2). The minerals in these ores mainly show euhedral-subhedral granular, anhedral granular and metasomatic textures. Various minerals occur in the Huxu deposit; the main metal minerals include natural gold, pyrite, galena, sphalerite, chalcopyrite, hematite and a very small amount of molybdenite. Non-metallic minerals primarily consist of quartz, with minor amounts of ankerite, calcite, muscovite or sericite, apatite and fluorite. Commonly, sulfide contents in the quartz-sulfide type ores of the Huxu deposit are < 20%.

The wall rocks in the study area have suffered relatively strong alteration under the influence of mineralization; the main alteration types are silicification, hematitization, sericitization, chloritization, carbonatization and pyritization (Fig. 3), among which silicification and gold mineralization are closely related (Wang et al. 1998).

According to the ore structure and mineral metasomatism characteristics, the mineralization of the deposit can be divided into four stages (Fig. 4). The first stage is the quartz-pyrite stage (S1). The primary minerals in this stage consist of quartz and pyrite (Py1), with the pyrite displaying a relatively clean appearance and exhibiting a euhedral-subhedral texture (Fig. 5a-g). The second stage is the

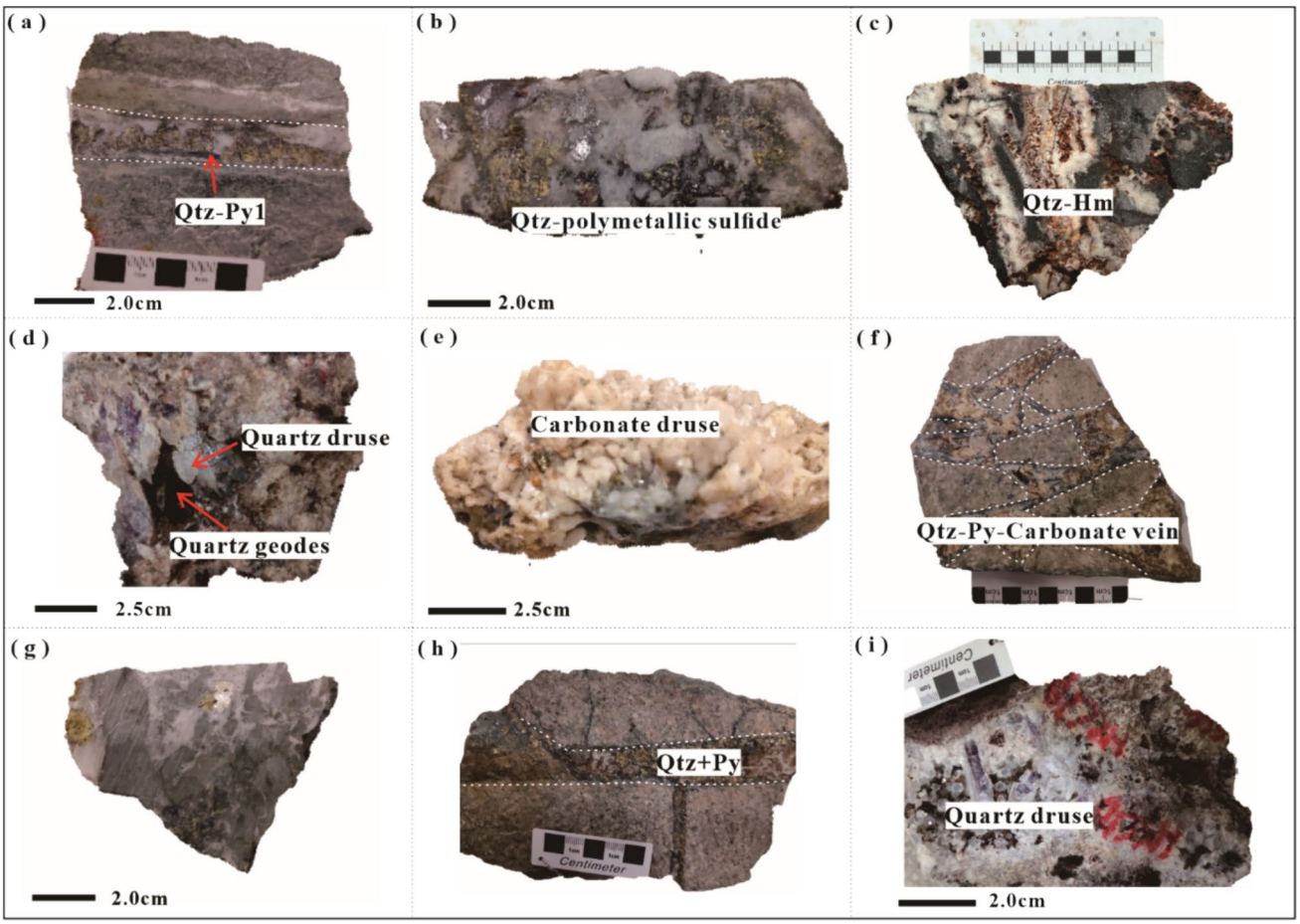

Fig. 2 Ore structural characteristics of the Huxu Au-dominated polymetallic deposit. **a** Quartz-pyrite vein cutting through the surrounding rock; **b** quartz-polymetallic sulfide veins; **c** quartz, chalcedony and large quantities of hematite; **d** quartz geodes; **e** carbonate cluster with euhedral sulfides on their surfaces; **f** brecciated porphyry cemented by quartz-pyrite-carbonate mineral; **g** brecciated porphyry cemented by quartz vein; **h** quartz-pyrite vein cutting through porphyry; **i** quartz druse. Qtz, quartz, Py, pyrite, Hm, hematite

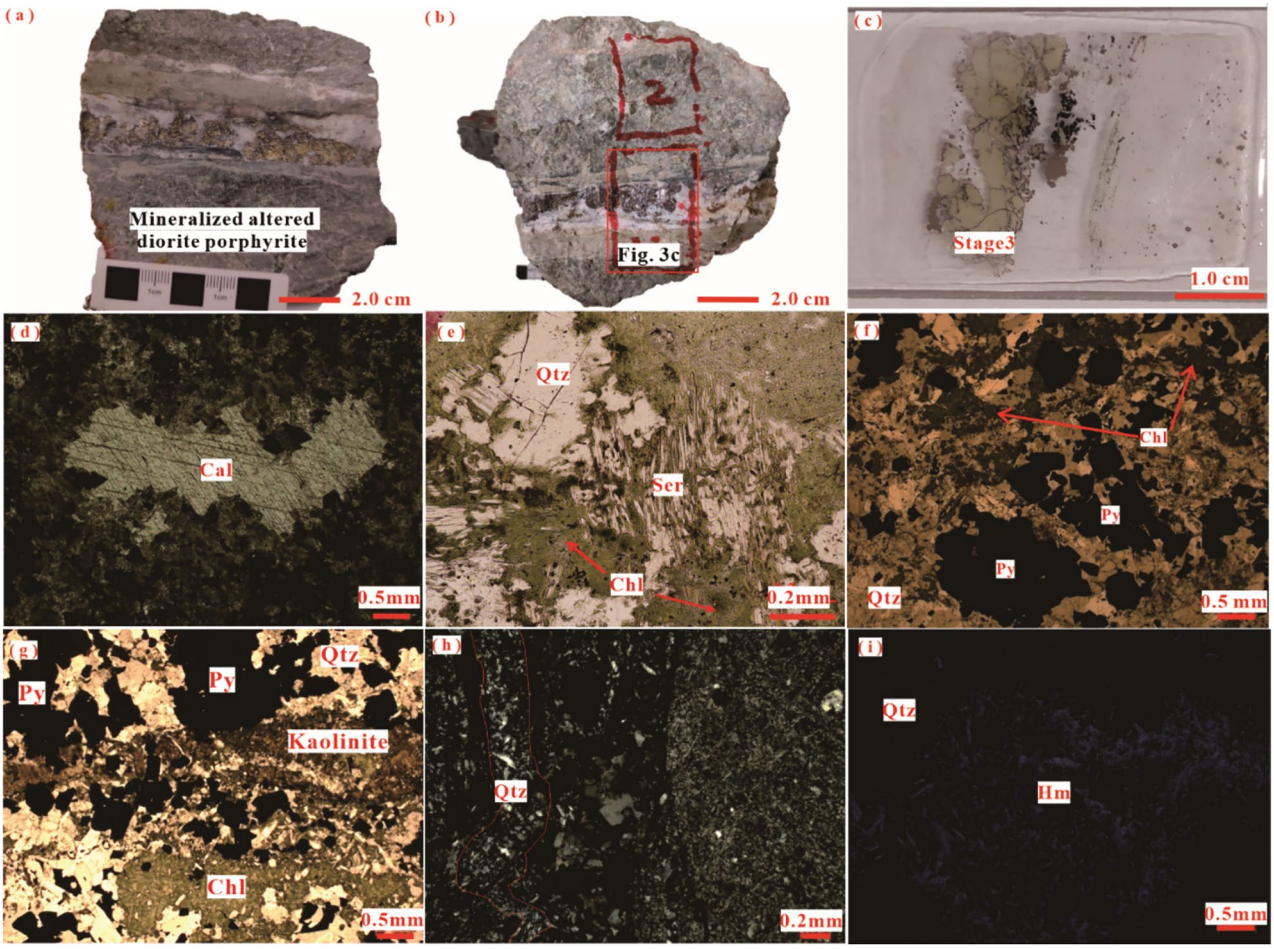

Fig. 3 Alteration characteristics of the Huxu gold polymetallic deposit. **a** Quartz-pyrite vein cutting through the surrounding rock; **b** slice position; **c** quartz-polymetallic sulfide slice; **d** carbonatization; **e** sericitization and chloritization; **f** pyritization and chloritization; **g** kaolinization and chloritization; **h** silicification; **i** hematitization. Py, pyrite, Qtz, quartz, Hm; hematite; Cal, calcite; Ser, sericite; Chl, chlorite

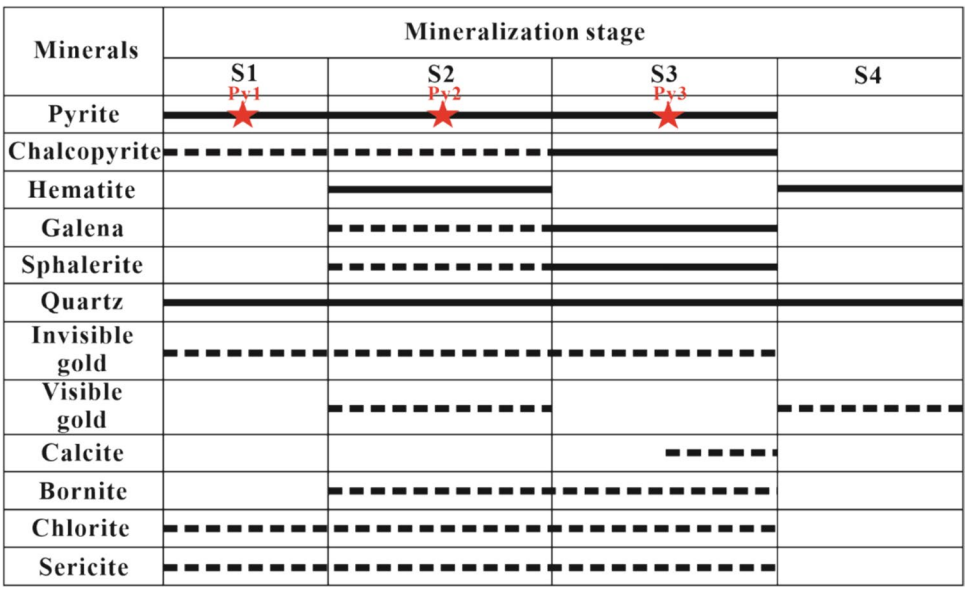

Fig. 4 Mineral paragenetic sequence for the Huxu Au-dominated polymetallic deposit. Solid lines indicate high contents, and dashed lines indicate low contents. S1 = stage 1, S2 = stage 2, S3 = stage 3, S4 = stage 4

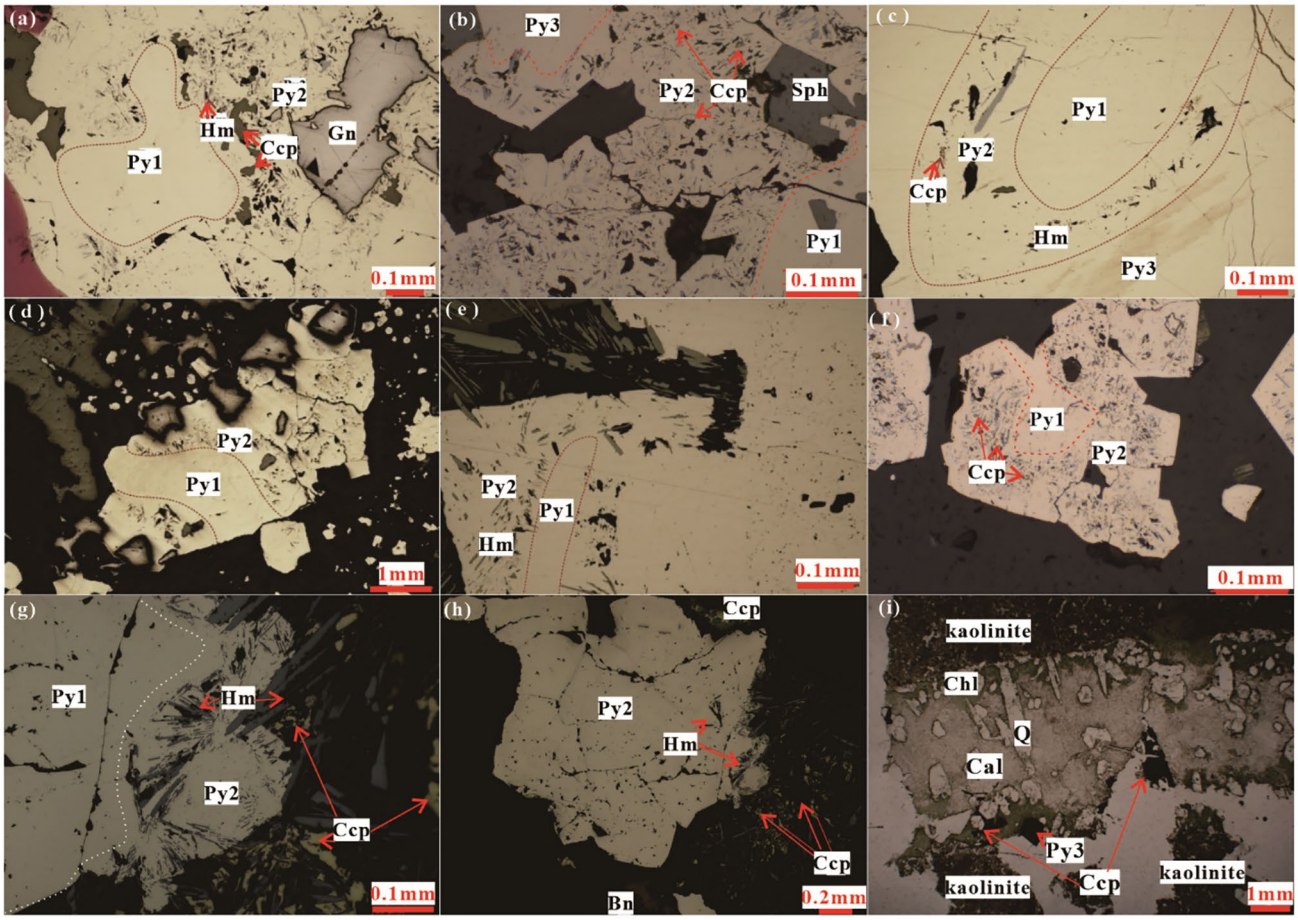

Fig. 5 Mineral composition of the Huxu Au-dominated polymetallic deposit. Py, pyrite; Ccp, chalcopyrite; Gn, Galena; Qtz, quartz; Hm, hematite; Cal, calcite

quartz-hematite-pyrite stage (S2). Hematite in this stage is needle-like and occurs as inclusion in the pyrite (Py2). Small amounts of sphalerite, chalcopyrite and silicate mineral inclusions in the pyrite can also be observed in this stage (Fig. 5a-h). The third stage is the quartz-polymetallic sulfide stage (S3), in which pyrite, sphalerite, galena and chalcopyrite can be easily observed. Pyrite (Py3) in this stage is relatively pure and can either grow along the edges of Py2 or in the form of euhedral crystals (Fig. 5b, c). A small amount of calcite can also be observed in this stage (Fig. 5i). The fourth stage is quartz-hematite stage (S4), in which no sulfide is found. The quartz grains from this stage are porous, with some quartz in the form of cryptocrystalline chalcedony.

4 Samples and analytical methods

Before the compositional analysis, the samples were photographed and observed in detail, and then representative samples were selected to make polished slices. The structures, textures and mineral compositions of the ores were determined based on macroscopic and microscopic observation, and representative mineral grains were selected. The backscattering and energy spectrum analyses were carried out by scanning electron microscopy (ZEISS Sigma 300VP) in the State Key Laboratory of Nuclear Resources and Environment, of East China University of Technology to further determine the inclusions and altered minerals for further analysis.

4.1 *In-situ* trace element analysis

Trace element analysis of sulfide was conducted using LA-ICP-MS at the Wuhan Sample Solution Analytical Technology Co., Ltd., Wuhan, China, and Nanjing FocuMS Technology Co. Ltd., Nanjing, China. The experiment in Wuhan laboratory used the Geolaspro laser ablation system, which was equipped with COMPexPro 102 ArF excimer laser (wavelength of 193 nm, maximum energy 200 MJ) and a MicroLas optical system, while the experiment in Nanjing laboratory used the combination of Teledyne Cetac Technologies Analyte Excite laser-ablation system (Bozeman,

Montana, USA) and Agilent Technologies 7700 × quadrupole ICP-MS (Hachioji, Tokyo, Japan). The spot size of the laser is 40 μm, and the frequency is 5 Hz. Helium is used as the carrier gas and argon as the compensation gas. It is mixed with the carrier gas through the T-connector and enters the ICP. The laser ablation system in Wuhan laboratory includes a "wire" signal smoothing device (Hu et al 2015). During the analysis process, each sample has about 20–30 s of background acquisition before analysis followed by 50 s of sample data acquisition. Each acquisition in Nanjing laboratory includes 20 s of background (gas blank) and then 40 s of sample acquisition with a spot diameter of 40 um and a repetition rate of 5 Hz. In addition, both experiments used USGS polymetallic sulfide press sheet MASS-1 as an unknown sample to verify the accuracy of the calibration method. An external calibration using synthetic basalt glass GSE-1G was also used in conjunction with the Nanjing laboratory. In terms of data analysis software, the experiment in Wuhan laboratory uses ICP-MS Data Cal software based on Excel to perform offline selection and integration of background and analysis signals, time-drift correction and quantitative calibration of trace element analysis (Liu et al. 2008), and the operating conditions, instrument configuration and data reduction methods are the same as those described by Zong et al. (2017).

4.2 *In-situ* S-Pb isotope analysis

Sulfur isotopic ratios of sulfides (pyrite) were conducted by LA-MC-ICP-MS at Nanjing FocuMS Technology Co., Ltd. Teledyne Cetac Technologies Analyte Excite laser-ablation system (Bozeman, MT, USA) and Nu Instruments Nu Plasma II MC-ICP-MS (Wrexham, Wales, UK) were combined for the experiments. Adjustable source slit of Nu Plasma II was set to 50 μm width to achieve pseudo-resolution resolving power (5%–95%) > 8000, and the magnet was set to left edge of peak (interference-free shoulder). The 193-nm ArF excimer laser, homogenized by a set of beam delivery systems, was focused on the surface with fluence of 2.5 J/cm^2. Each acquisition incorporated 30 s background (gas blank) followed by spot diameter of 35 um at 5 Hz repetition rate for 40 s. Helium (800 ml/min) was applied as carrier gas to efficiently transport aerosol out of the ablation cell and was mixed with argon (~0.8 l/min) via T-connector before entering ICP torch. Integration time of Nu Plasma II was set to 0.3 s (equating to 115 cycles during the 35 s). Natural Wenshan pyrite ($\delta^{34}S = +1.1\%$ V-CDT) was used as external bracketing standard every fourth analysis. Pressed powder pellets of pyrite GBW07267 and chalcopyrite GBW-07268 ($\delta^{34}S = +3.6\%, -0.1\%$, respectively, from National Research Center for Geoanalysis, China) and fine-grained sphalerite SRM 123($\delta^{34}S = +17.5\%$, from National Institute of Standards and Technology, USA) were treated as quality control. The long-term reproducibility of $\delta^{34}S$ is better than 0.5% (1 SD).

In-situ lead isotope analyses of sulfide (pyrite) were performed on a Neptune Plus MC-ICP-MS (Thermo Fisher Scientific, Bremen, Germany) equipped with a Geolas HD excimer ArF laser ablation system (Coherent, Göttingen, Germany) at the Wuhan Sample Solution Analytical Technology Co., Ltd., Hubei, China. In the laser ablation system, helium was used as the carrier gas for the ablation cell and was mixed with argon (makeup gas) after the ablation cell. The spot diameter ranged from 44 to 90 μm dependent on Pb signal intensity. The pulse frequency was from 4 to 10 Hz, but the laser fluence was kept constant at ~ 5 J/cm^2. A new signal-smoothing and mercury-removing device was used downstream from the sample cell to efficiently eliminate the short-term variation of the signal and remove the mercury from the background and sample aerosol particles (Hu et al. 2015). The Neptune Plus was equipped with nine Faraday cups fitted with 1011Ω resistors. Isotopes ^{208}Pb, ^{207}Pb, ^{206}Pb, ^{204}Pb, ^{205}Tl, ^{203}Tl and ^{202}Hg were collected in Faraday cups using static mode. The mass discrimination actor for Pb was determined using a Tl solution nebulized at the same time as the sample, using an Aridus II desolvating nebulizer. The mass fractionation of Pb isotopes was corrected by ^{205}Tl/^{203}Tl with the exponential law. Note that the optimized values of ^{205}Tl/^{203}Tl, which were calibrated by measuring two Pb isotope standards, MASS-1 (USGS) and Sph-HYLM (sphalerite, in-house standard), replaced the natural Tl isotopic composition for the mass fractionation correction of Pb isotopes. The ^{202}Hg signal was used to correct the remaining ^{204}Hg interference on ^{204}Pb, using the natural ^{202}Hg/^{204}Hg ratio (0.2301). In addition, the mass fractionation of ^{204}Hg/^{202}Hg was corrected by the ^{205}Tl/^{203}Tl normalization. In this case, we assumed identical mass fractionation factors for ^{204}Hg/^{202}Hg and ^{205}Tl/^{203}Tl. Sph-HYLM was used to monitor the precision and accuracy of the measurements after ten sample analyses over the entire period of analysis. The obtained accuracy is estimated to be ≥ ± 0.2% for ^{208}Pb/^{204}Pb, ^{207}Pb/^{204}Pb and ^{206}Pb/^{204}Pb compared to the solution value by MC-ICP-MS with a typical precision of 0.4% (2σ). More detail of the *in-situ* Pb isotopic ratios analysis was described in Zhang et al. (2016). All data reduction for the MC-ICP-MS analysis of Pb isotope ratios was conducted using "Iso-Compass" software (Zhang et al. 2020).

5 Results

Three generations of pyrite from the Huxu Au-dominated polymetallic deposit have been identified: Py1 in stage 1, Py2 in stage 2 and Py3 in stage 3. In total, 94 spot analyses were performed using LA-ICP-MS to examine trace elements in pyrite (Py1 = 33, Py2 = 37, Py3 = 24). Additionally,

30 spot analyses were conducted with LA-MC-ICP-MS to study sulfur isotopes in pyrite (Py1 = 7, Py2 = 11, Py3 = 12), while ten more spot analyses were carried out for lead isotopes using LA-MC-ICP-MS in pyrite (Py1 = 1, Py2 = 6, Py3 = 3).

5.1 Trace elements of pyrite

The trace element compositions of pyrite of different stages (Py1–Py3) are listed in supplementary Table 1 and shown in Fig. 6. Pyrite from different generations shows significant variation in trace element compositions.

A variety of trace elements can be detected in Py1. In comparison to Py2 and Py3, these pyrites exhibit the highest concentrations of Cu (average 410.04 ppm) and Ni (average 15.01 ppm) but relatively lower concentrations of Au (average 0.18 ppm), As (average 316.70 ppm), Ag (average 8.64 ppm), Pb (average 581.31 ppm), Zn (average 82.96 ppm), Bi (average 55.80 ppm) and Co (average 75.74 ppm).

Py2 has the highest concentrations of As (average 470.89 ppm), Ag (average 25.49 ppm), Pb (average 3650.98 ppm), Zn (average 312.15 ppm), Bi (average 92.58 ppm), Co (average 148.60 ppm), W (average 27.27 ppm) and Al (average 103.31 ppm). These pyrites have lower concentrations of Cu (average 283.35 ppm) and Ni (average 1.46 ppm) and higher concentrations of Au (average 0.32 ppm) than Py1.

Py3 has the highest concentrations of Au (average 0.68 ppm). However, it has lower concentrations of other elements compared to Py2. The concentrations of Sb, Ni, W, Sc, V, Ti and U in Py3 are extremely low (average < 5 ppm).

The concentrations of Ag, Pb, Zn, Bi, Co, U and Sc initially increased and then decreased from early to late (Py1 → Py2 → Py3). Similarly, As, Al, W, Ti and V also displayed a trend of increasing and then decreasing, but with concentrations of these elements of Py3 slightly higher than those of Py1 (Fig. 6). The concentrations of Cu and Ni decreased gradually, whereas those of Au and Sb increased gradually. Notably, an increase in the concentration of Au was accompanied by a high concentration of As (Fig. 7).

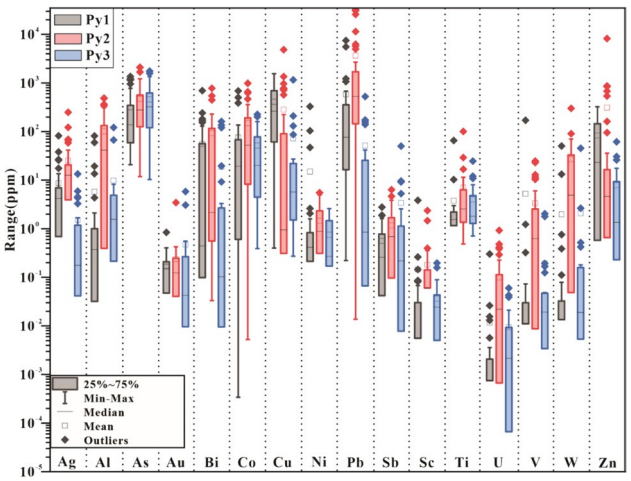

Fig. 6 Box plots for trace elements in pyrite from the Huxu Au-dominated polymetallic deposit (ppm)

5.2 *In-situ* S-Pb isotope

In-situ sulfur and lead isotope values of pyrite from the Huxu Au-dominated polymetallic deposit are presented in Tables 1 and 2, respectively. *In-situ* $\delta^{34}S$ values of pyrite from different generations are similar, with those of Py1 ranging from − 0.7% to + 3.2%, Py2 from − 1.5% to 4.2% and Py3 from − 0.3% to + 4.3%. As a whole, the $\delta^{34}S$ values of these pyrites show a narrow range from − 1.5% to + 4.3%, with an average value of 1.72%, closely approximating zero. *In-situ* lead isotope ratios of pyrites in the deposit display $^{208}Pb/^{204}Pb$ values ranging from 38.462 to 38.684, $^{207}Pb/^{204}Pb$ values ranging from 15.579 to 15.768 and $^{206}Pb/^{204}Pb$ values ranging from 18.037 to 18.241.

6 Discussion

6.1 Trace element distributions in pyrite

Pyrite, as the most common product in hydrothermal activities, often contains Au, Ag, Pb, Zn, Cu, Co, Ni, As, Sb, Se, Te, Bi and other trace elements (Bi et al. 2004; Gong et al. 2011; Wang et al. 2021; Zhang et al. 2022). These trace elements exist in different forms, including (1) invisible solid solutions within the pyrite lattice, (2) invisible mineral nanoparticles and (3) visible micrometer-scale mineral inclusions (Zhang et al. 2022).

Co, Ni and As are always occur as solid solutions in pyrite (Fan et al. 2018; Zhang et al. 2022).

The trace element maps show that the distribution of their content is relatively uniform (Fig. 7). Additionally, the flat patterns of the LA-ICP-MS time-resolved signal spectra of As, Co, Ni and their consistent spectral patterns to those of Fe and S suggest that these elements probably occur as solid solutions in the pyrite crystal lattice in the Huxu deposit (Fig. 8a) (Fan et al. 2018; Zhang et al. 2022). In the trace element maps, the high-content areas of Cu, Pb and Zn elements are spatially overlapped with sulfide inclusions in pyrite (Fig. 7), indicating distribution of these elements is mainly controlled by mineral inclusions, such as chalcopyrite, galena and sphalerite. In the time-resolved spectrograms, sharp peaks of signals for these elements can be observed (Fig. 8b, c), further supporting their presence in the form of mineral inclusions in pyrite. In the Huxu

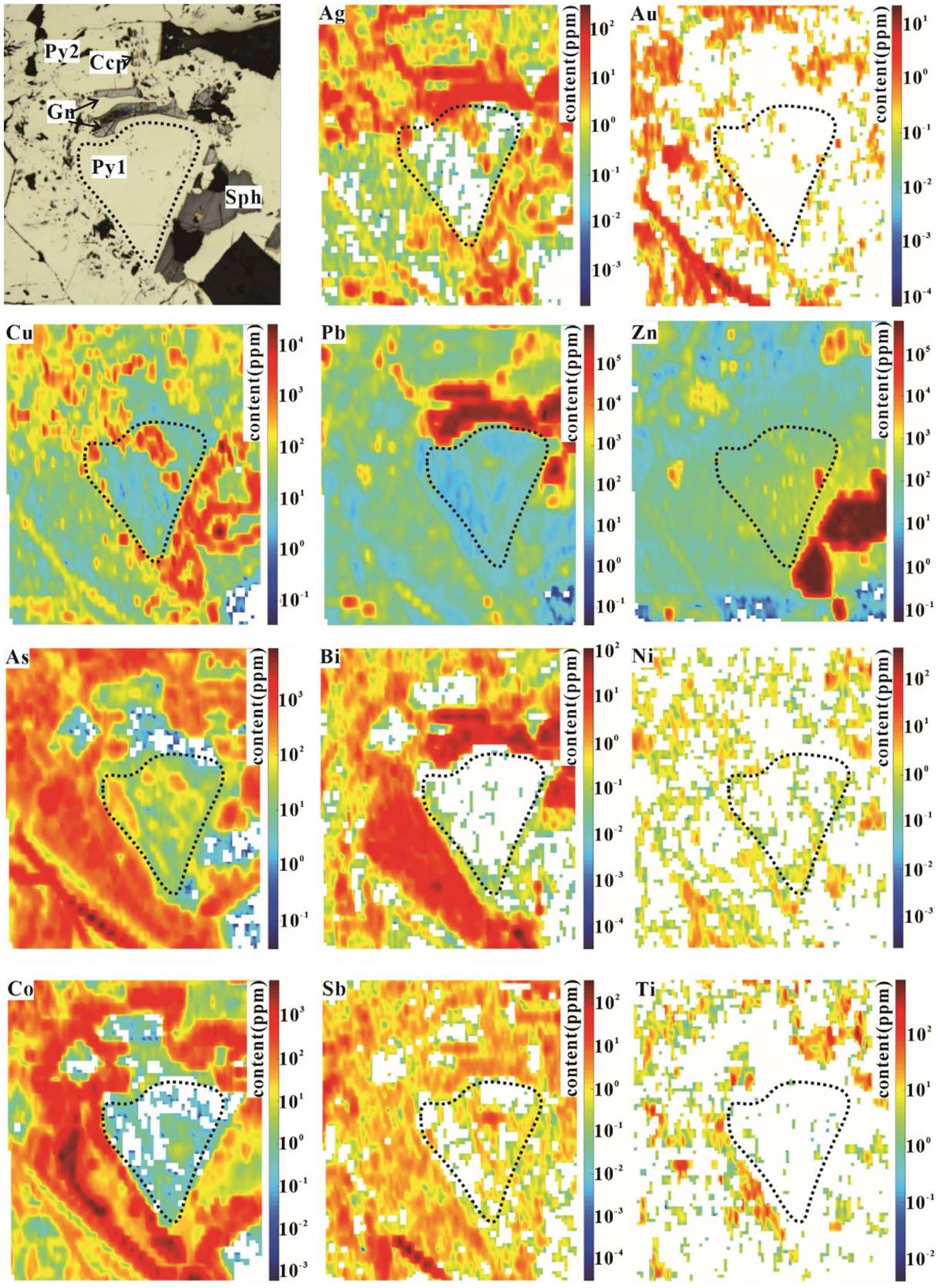

Fig. 7 Trace element spatial distribution of pyrite from the Huxu Au-dominated polymetallic deposit (ppm). Py, pyrite; Ccp, chalcopyrite; Gn, galena; Qtz, quartz; Sph, sphalerite

Table 1 *In-situ* isotopic compositions of pyrite from the Huxu Au-dominated polymetallic deposit

No.	Stage	$\delta^{34}S_{V-CDT}$	2SE
CHX01a-1-04	1	− 0.1	0.3
CHX01a-1-05	1	− 0.2	0.3
CHX01a-3-06	1	− 0.7	0.3
CHX01a-3-07	1	0.2	0.3
CHX01c-2-14	1	2.5	0.2
CHX01a-1-01	2	− 0.5	0.2
CHX01a-1-02	2	0.6	0.3
CHX01a-1-03	2	0.0	0.3
CHX01a-3-12	2	− 1.5	0.3
CHX01a-3-13	2	0.4	0.3
CHX01c-2-15	2	4.0	0.3
CHX01c-2-16	2	4.2	0.2
CHX01c-4-23	2	2.5	0.2
CHX01c-1-28	2	4.1	0.3
CHX01c-1-29	2	2.8	0.3
CHX01c-1-30	2	2.5	0.3
CHX01a-3-08	3	1.6	0.3
CHX01a-3-09	3	− 0.3	0.3
CHX01a-3-10	3	0.8	0.3
CHX01a-3-11	3	1.2	0.2
CHX01c-2-17	3	4.3	0.3
CHX01c-2-18	3	3.8	0.2
CHX01c-2-19	3	2.0	0.2
CHX01c-3-20	3	1.8	0.2
CHX01c-3-21	3	2.9	0.3
CHX01c-3-22	3	2.3	0.2
CHX01c-4-24	3	3.2	0.2
CHX01c-4-25	3	2.4	0.2

Table 2 *In-situ* Pb isotopic data of pyrite from the Huxu Au-dominated polymetallic deposit

No.	Stage	$^{208}Pb/^{204}Pb$	$^{207}Pb/^{204}Pb$	$^{206}Pb/^{204}Pb$
CHX01a-04	1	38.580	15.614	18.183
CHX01a-08	2	38.574	15.613	18.183
CHX01a-09	2	38.590	15.617	18.187
CHX01a-10	2	38.592	15.618	18.191
CHX01a-11	2	38.591	15.621	18.196
CHX01a-24	2	38.568	15.611	18.186
CHX01a-27	2	38.574	15.611	18.188
CHX01a-20	3	38.462	15.579	18.163
CHX01a-23	3	38.625	15.631	18.208
CHX01a-33	3	38.684	15.654	18.241

Au-dominated polymetallic deposit, there are clear positive correlations among Ag, Bi and Sb with Pb (Fig. 9a, b). In the time-resolved spectrogram, an identical trend could be observed for Ag, Bi, Sb and Pb (Fig. 8b, c). These collectively suggest that Ag, Bi and Sb predominantly exist as solid solutions within galena inclusions in pyrite (Shannon 1976; Cook et al. 1998; Wang et al. 2021).

Gold could occur as solid solution (Au^+) or gold-bearing mineral inclusions (such as native gold, gold-bearing telluride, etc.) in pyrite (Tauson 1999; Reich et al. 2005; Li et al. 2010). In the Huxu Au-dominated polymetallic deposit, there is no correlation between Au and Te (Fig. 9c), and no telluride inclusions are found under the microscope. Therefore, Au in pyrite should not exist in the form of gold-bearing telluride. It is contended that the presence of gold (Au) in pyrite crystal lattice is intricately controlled by the existence of arsenic (As) within the pyrite, since the introduction of As into pyrite would result in the distortion of its octahedral structure, consequently facilitating the incorporation of gold into pyrite crystal lattice (Reich et al. 2005). In the Huxu Au-dominated polymetallic deposit, there is a positive correlation between Au and As, and the Au content is lower than the maximum solubility of gold in pyrite (Fig. 9d). In the LA-ICP-MS time-resolved spectrogram, the profile of Au shows no peak signals caused by gold-bearing inclusions (Fig. 8d). Therefore, we believe that the invisible gold in the Huxu Au-dominated polymetallic deposit mainly exists in the form of solid solution (Au^+) in the pyrite lattice.

6.2 Fluid and metal sources

6.2.1 Fluid source

The S isotopes in sulfide serve as an indicator of the sulfur source in the fluid and, consequently, indirectly reveals the origin of the fluid. Previous studies have demonstrated that the average sulfur isotope value of sulfides can serve as a rough estimation of sulfur isotope compositions of the ore-bearing hydrothermal solutions, especially when no sulfates are present (Ohmoto 1972). Different sources commonly exhibit distinct isotopic compositions. Commonly, fluids derived from seawater or marine sedimentary strata show notable positive $\delta^{34}S$ values; those from organic materials show obvious negative $\delta^{34}S$ values, while those from mantle show near-zero $\delta^{34}S$ values (Ohmoto 1986).

In the Huxu Au-dominated polymetallic deposit, the ores are mainly composed of pyrite, chalcopyrite, galena and sphalerite and are devoid of any sulfate. Thus, the sulfur isotopic composition of the sulfide could generally represent the sulfur isotopic composition of the fluid. In the frequency histogram of $\delta^{34}S$, $\delta^{34}S$ of pyrites from different stages all exhibits a relatively similar small range, with an overall range from –2% to 5%. This suggests that the sulfur and by inference the fluid in each stage have a similar source. The limited range of $\delta^{34}S$ values and near-zero average $\delta^{34}S$ values suggest that the sulfur involved in ore

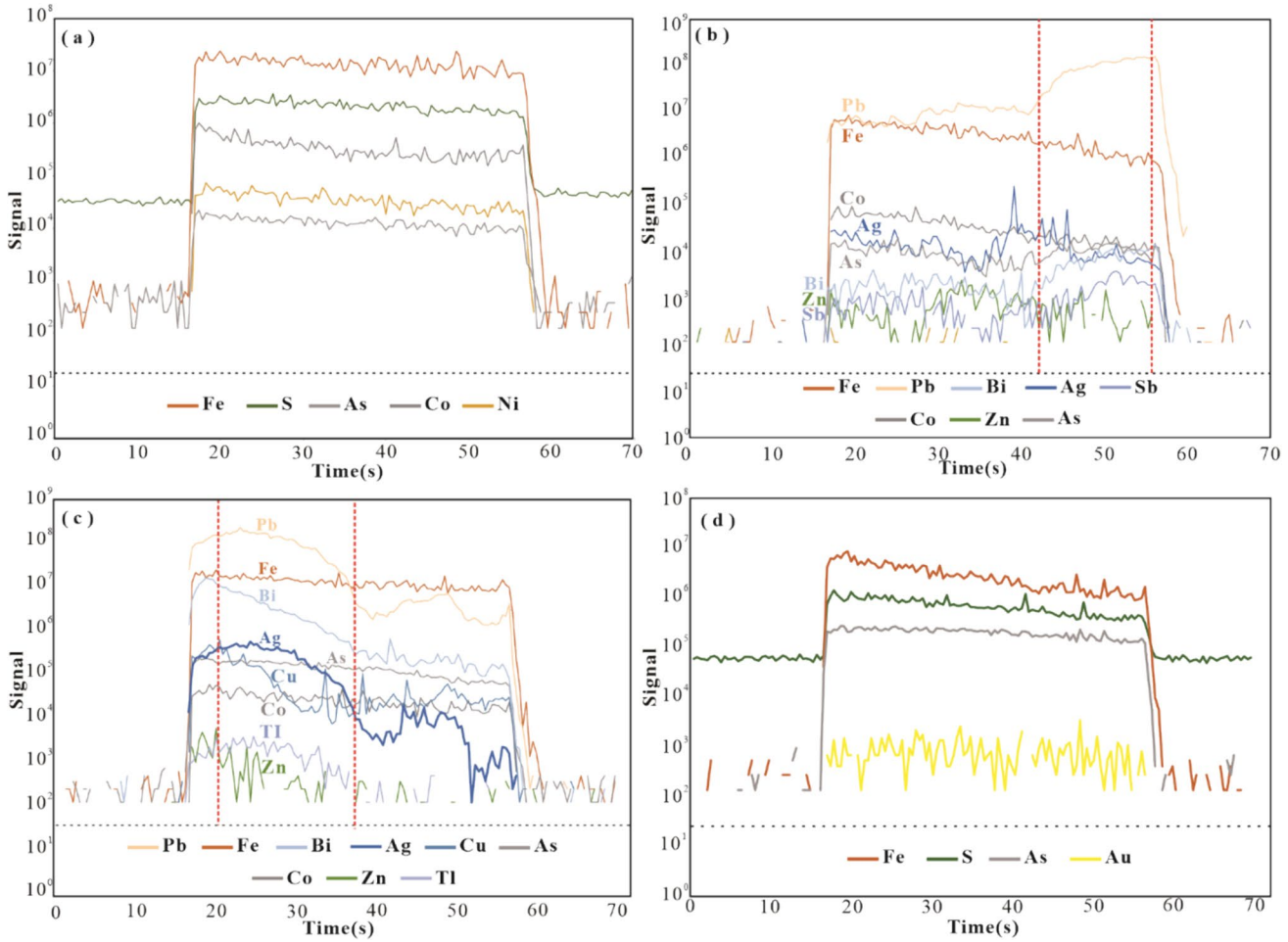

Fig. 8 Representative LA-ICP-MS time-resolved spectra for pyrite from the Huxu Au-dominated polymetallic deposit. **a** As, Co, Ni signals are smooth and parallel to Fe, S signals; **b** peak signals of Pb, Bi, Ag and Sb in the red dashed area indicate the presence of possible Pb-Bi-Ag-Sb inclusions; **c** peak signals of Pb, Bi, Ag, Cu and Sb in the red dashed area indicate the presence of possible Pb-Cu-Bi-Ag-Sb inclusions; **d** signals of Fe, S, As and Au

formation, and consequently the associated fluid, is unlikely to originate from sedimentary rocks. Instead, they are more likely derived from a magmatic source. Furthermore, the $\delta^{34}S$ values of pyrite in the Huxu Au-dominated polymetallic deposit are highly similar to those of sulfides in nearby magmatic-hydrothermal deposits such as the Dexing porphyry deposit (− 4%–3.1%; Zhou et al. 2012), Dongxiang deposit (0.3%–1.6%; Cai et al. 2016) and Yinshan deposit (1.7%–3.2%; Wang et al. 2013) (Fig. 10). This further confirms that sulfur and by inference the ore-forming fluid of the Huxu Au-dominated polymetallic deposit should be from magma.

The H-O isotopic composition serves as a reliable tracer for fluid origin. Here, we also compiled H-O isotope data published to further constrain the fluid sources of the Huxu Au-dominated polymetallic deposit. The H-O data for fluid inclusions enclosed in quartz from the Huxu Au-dominated polymetallic deposit are illustrated in Fig. 11. The δD values range from –70.1 to –84.4, and the $\delta^{18}O$ values range from 0.1 to 1.8, demonstrating generally low δD and $\delta^{18}O$ values (Wang et al. 1998). In the covariation diagram of δD and $\delta^{18}O$ (Fig. 11), the data concentrate below the magmatic water region, trending closer to the evolution line of meteoric water. This suggests that the ore-forming hydrothermal fluid may have multiple sources, predominantly consisting of magmatic water with minor meteoric water involved.

6.2.2 *Metal source*

The pyrites from the Huxu Au-dominated polymetallic deposit exhibit average $^{208}Pb/^{204}Pb$ of 38.556, $^{207}Pb/^{204}Pb$ of 15.667 and $^{206}Pb/^{204}Pb$ of 18.173. These pyrites have uniform radiogenic Pb isotopic compositions, indicating that the metals in all stages should have a similar source. The lead isotopic compositions of pyrite from the Huxu Au-dominated polymetallic deposit closely resemble those

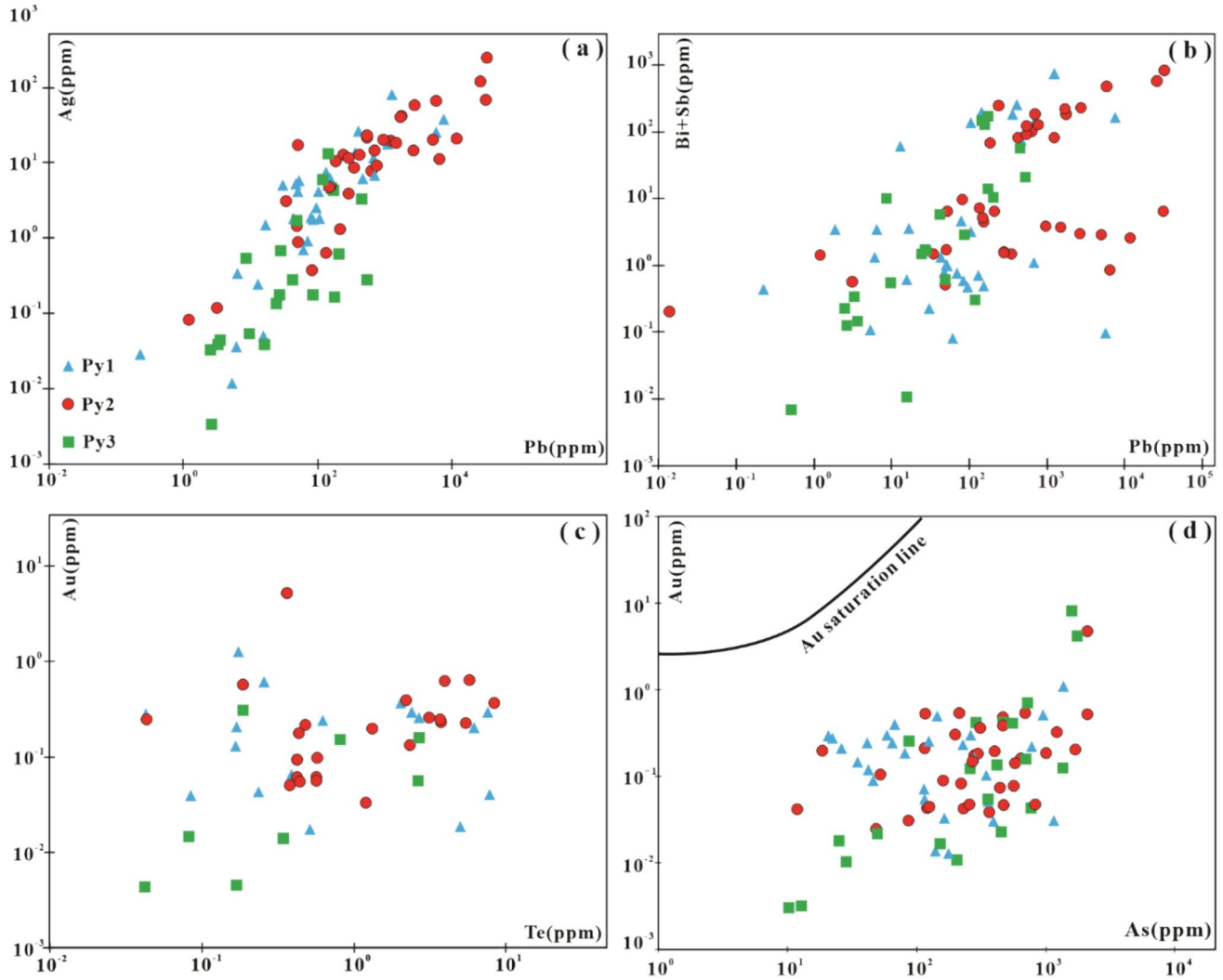

Fig. 9 Trace element correlation for different generations of pyrite from the Huxu Au-dominated polymetallic deposit **a** Ag-Bi; **b** (Bi + Sb)–Pb; **c** Au-Te; **d** Au-As (the gold solubility curve from Reich et al. 2005 applies to Carlin-type and epithermal deposits)

of the magmatic-hydrothermal Yinshan deposit in the adjacent area, indicating a shared source for their metals (Fig. 12). Considering the metals of the Yinshan deposit are believed to originate from magma (Wang et al. 2013), we contend the metals of the Huxu Au-dominated polymetallic deposit also have a magmatic origin. In addition, the lead isotope ratios of the pyrite from the Huxu Au-dominated polymetallic deposit are almost consistent with those of the Yanshanian trachyandesitic rocks in the adjacent Shengyuan Basin (Shu et al. 2017) and Yanshanian granodiorite porphyry in the Dongxiang deposit (Fig. 12) (Ouyang 2015) but markedly different from those of the Shuangqiaoshan formation. This further suggests that lead and other metals (e.g., Au, Cu and Zn) of the Huxu Au-dominated polymetallic deposit likely originated from the Yanshanian magma.

6.3 Metal precipitation mechanism

Metals (Au, Pb, Zn, etc.) usually exist in the form of complexes during the migration and deposition processes. Au is generally complexed with HS^-, while Pb and Zn are mostly complexed with Cl^- under typical hydrothermal conditions. Changes in the physical and chemical conditions of the ore-forming fluid, such as temperature, pH, fO_2 and fS_2, could cause the decomposition of metal complexes in it and precipitation of metals (Zhang et al. 1997a, b; Schaarschmidt et al. 2021; Cao et al. 2023). The processes that lead to changes in the physical and chemical conditions of the ore-forming fluid mainly include fluid boiling, fluid mixing, water-rock interaction or cooling (e.g., Schaarschmidt et al. 2021; Cao et al. 2023). Based on previous studies, the precipitation of visible gold (Au) in the Huxu Au-dominated polymetallic

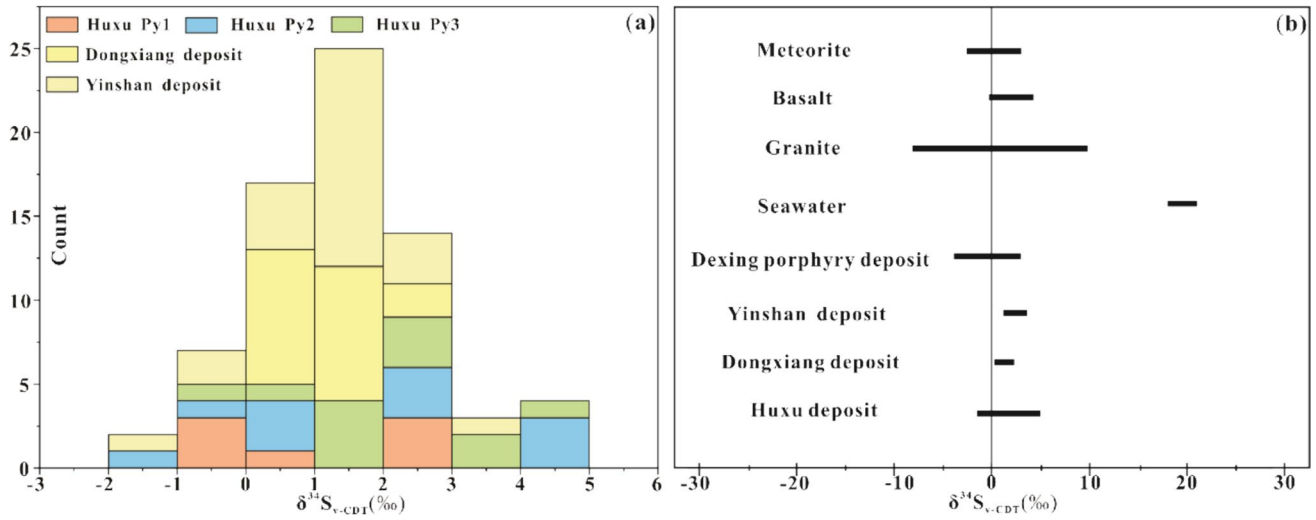

Fig. 10 **a** Sulfur isotope histogram; **b** $\delta^{34}S$ feature comparison chart (data of the meteorite, basalt, granite and seawater are from Rollinson (1993) and references therein; data of the Dongxiang deposit, Yinshan deposit are from Cai et al. (2016) and Wang et al. (2013), respectively

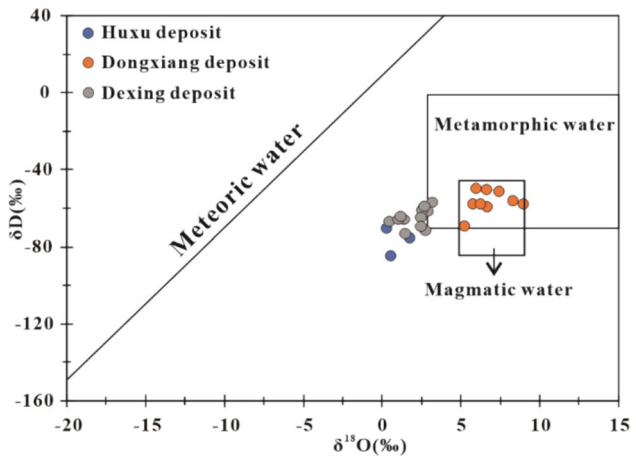

Fig. 11 δD (%) versus $\delta^{18}O$ (%) of the Huxu Au-dominated polymetallic deposit (data of the Huxu Au-dominated polymetallic deposit, Dexing deposit and the Dongxiang deposit are from Wang et al. (1998), Yang et al. (2016) and Cai et al. (2016), respectively; field of magmatic and metamorphic water and SMOW are sourced from Taylor (1974)

deposit primarily occurs in the quartz-hematite-pyrite stage (S2) and the quartz-hematite stage (S4), while the precipitation of Pb and Zn primarily occur in the quartz-polymetallic sulfide stage (S3) (Wang et al. 1998). In the following discussion, we focus on the mineral precipitation mechanism during stages 2 to 4, during which visible gold and Pb-Zn precipitated.

6.3.1 Precipitation mechanism of gold

The trace elements and textures of pyrite can offer information on the chemical evolution of hydrothermal fluid and thus have implications for elucidating the metal precipitation process (Maslennikov et al. 2009; Roman et al. 2019; Schaarschmidt et al. 2021). As shown in Fig. 5, numerous acicular or blade-like hematites can be observed in the Py2. Py2 displays porous texture, and numerous minute inclusions of chalcopyrite, sphalerite and silicate can be observed, indicating that rapid crystallization may have occurred (Gamarra-Urrunaga et al. 2013). Furthermore, brecciform ores have developed in the area, and the breccias are often cemented by quartz-sulfide veins (Fig. 3f, g). These characteristics are consistent with those observed in pyrite for deposits under condition of fluid boiling (Roman et al. 2019; Ni et al. 2020). Thus, we propose that fluid boiling occurred at stage 2 of Huxu deposit. The trace elements of pyrite seem also to support the above proposal. Py2 has the highest As, Ag and Pb contents among the analyzed pyrites, consistent with the chemical characteristics of pyrites formed in boiling environment (Roman et al. 2019). Based on previous studies, Te is less likely to enter pyrite under more oxidizing conditions, and Te contents have a negative correlation with fO_2 (Keith et al. 2018). In Huxu Au-dominated polymetallic deposit, the Te contents of pyrites decrease from Py1 (0.894 ppm) to Py2 (0.396 ppm) and increase in Py3 (0.543 ppm). The decrease in Te content in Py2 at stage 2 implies a possible increase in fO_2 of the fluid, which is also evidenced by the occurrence of hematite at this stage. Considering fluid boiling would increase fO_2, the lower Te content in Py2 may indirectly suggest fluid boiling during this stage. Moreover, Schaarschmidt et al. (2021) proposed that the Ag, As, Cu and As/Sb ratios in pyrite may indicate whether pyrite is the product of fluid-boiling. By comparing the trace element characteristics of Py1 to Py3 of the Huxu Au-dominated polymetallic deposit, it was observed that the data of Py2 are mainly plotted in

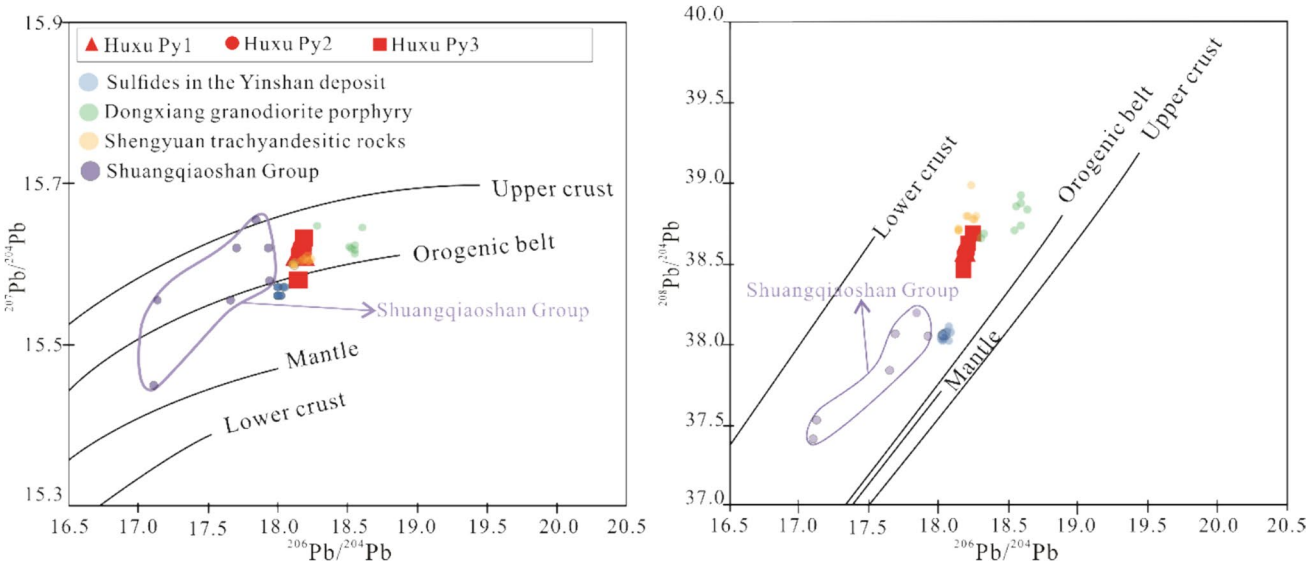

Fig. 12 Lead isotope compositions of the Huxu Au-dominated polymetallic deposit [reference lines of upper crust, orogenic belt, mantle and lower crust are from Zartman et al. (1981); data of the Yinshan deposit, Dongxiang granodiorite porphyry, Shengyuan trachyandesitic rocks and Shuangqiaoshan group are from Wang et al. (2013), Ouyang (2015), Shu et al. (2017) and Lu et al. (2005), respectively. The lead isotope compositions of Dongxiang granodiorite porphyry, Shengyuan trachyandesitic rocks and the pyrite of ores from the Yinshan deposit are also shown for comparison

the fluid boiling region, which further supports the fluid boiling during the stage 2 (Fig. 13). In reality, as a typical fault-controlled deposit (Fig. 1c), the earthquake-induced fault-valve processes could frequently result in fluid boiling (Sibson 1987). Taken together, we speculate that fluid boiling should have occurred during stage 2. The fluid boiling should also be the primary reason for the precipitation of metals, especially native gold, during this stage, since fluid boiling would decrease H_2S of the fluid and thus decompose the Au-S complexes [e.g., Au $(HS)_2^-$].

Apart from stage 2, native gold also precipitated in stage 4. Distinct from the S2 stage, no pyrite or other sulfides, are observed in the stage 4 ores. Instead, large amount of hematite and cryptocrystalline chalcedony occurred in this stage (Fig. 2c), which suggests low temperature and high fO_2 for the fluid. Considering the H-O isotopic characteristics (Fig. 11), we speculate that there was an infiltration of low-temperature and oxidized meteoric water during the S4 stage. The involvement of meteoric water should lead to a rise in fO_2 and decrease

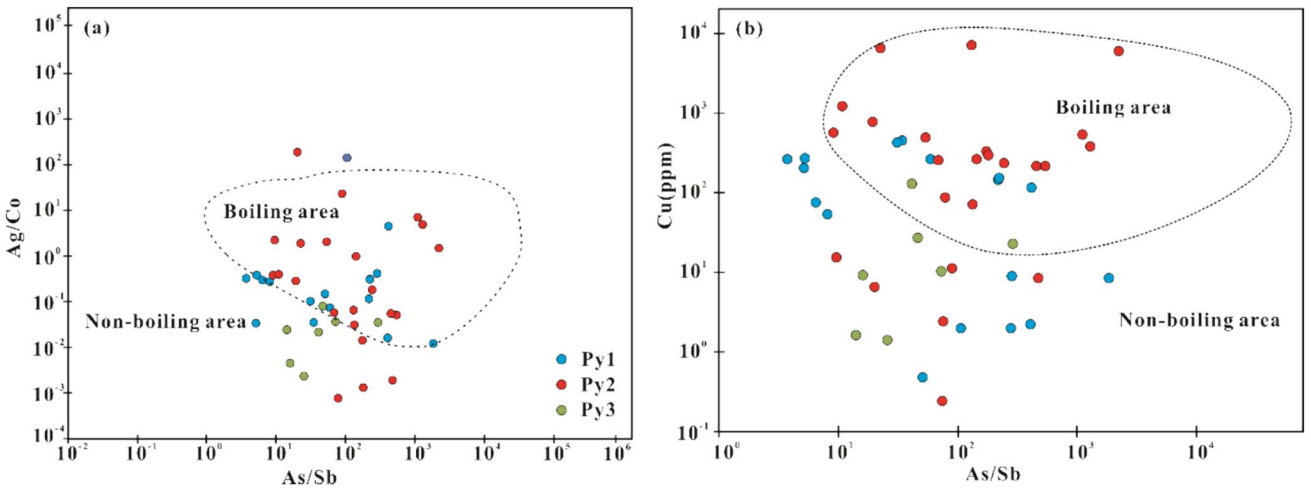

Fig. 13 Trace elements of pyrite indicate the possible boiling process. The areas of boiling and non-boiling are from Schaarschmidt et al. (2021b)

in fluid temperature, which subsequently promotes the precipitation of native gold. However, a further study is necessary to clarify the detailed process of the gold precipitation in this stage.

6.3.2 Precipitation mechanism of lead and zinc

Lead and zinc mainly precipitated during stage 3 and thus information related to fluid evolution could be recorded by Py3. In contrast to Py1 and Py2, Py3 is relatively clean, and there nearly no mineral inclusions are enclosed. The Pb and Zn mainly occur as galena and sphalerite co-precipitated with pyrite in quartz veins. These characteristics indicate that Py3 may be the product of slow crystallization under relatively stable physical and chemical conditions (Large et al. 2009; Moncada et al. 2012; Roman et al. 2019). Considering the occurrence of calcite in stage 3 (Fig. 5i), we speculate that an increase in pH may occur during stage 3. This speculation is supported by feldspar alteration of the wall rocks, since alteration of feldspar into clay mineral or sericite usually consumes H^+ in the hydrothermal solution (e.g., sericitization, kaolinization), leading to an increase in pH. Here, we infer that the increase in pH may be the reason that leads to the precipitation of Pb-Zn based on the present limited evidence, since the solubility of Pb and Zn in the fluid always decrease as pH increases (Shang et al. 2004). In summary, we propose water-rock interaction may be one of the reasons for Pb and Zn precipitation in stage 3, although more pieces of evidence are necessary.

6.4 Genetic type of the deposit

The geological characteristics, such as (1) the occurrence of ore bodies primarily as veins in subvolcanic or volcanic rocks (Fig. 1c) and (2) alterations including silicification, sericitization, chloritization (Fig. 3), with scarcity of high-temperature alteration combinations, indicate that the Huxu deposit should be an epithermal deposit. This contention is further supported by the relatively low homogeneous temperature of fluid inclusions in quartz (varying from 120 to 280 °C; Wang et al. 1998) and development of gas-liquid two-phase fluid inclusions instead of CO_2-bearing three-phase fluid inclusions (Wang et al. 1998; Chen et al. 2007).

The trace elements within pyrite can also provide valuable insights into the genetic type of the deposit. Ore deposits of different origins always display differences in the trace elements in their pyrite, since pyrite from various deposit types precipitates in different tectonic settings and/or physical-chemical conditions. The Co/Ni ratio is widely used to identify the origins of pyrite and, by inference, the genetic type of the deposit (Large et al. 2009; Reich et al. 2013). In general, sedimentary pyrite has a Co/Ni ratio < 1, while pyrite being magmatic with volcanic hydrothermal origins has a ratio > 1. Metamorphic hydrothermal pyrite tends to have a ratio similar to sedimentary pyrite, usually close to 1 (Gong et al. 2011). In the Huxu Au-dominated polymetallic deposit, the Co/Ni ratios of pyrite are generally > 1 (median 21.64, average 742.06), indicating their hydrothermal origin (Fig. 14). In addition, the mass fraction ratio of Co-Ni-As in pyrite is also commonly used to identify the source of pyrite, thereby indirectly indicating the genetic type and mineralization processes of the deposit

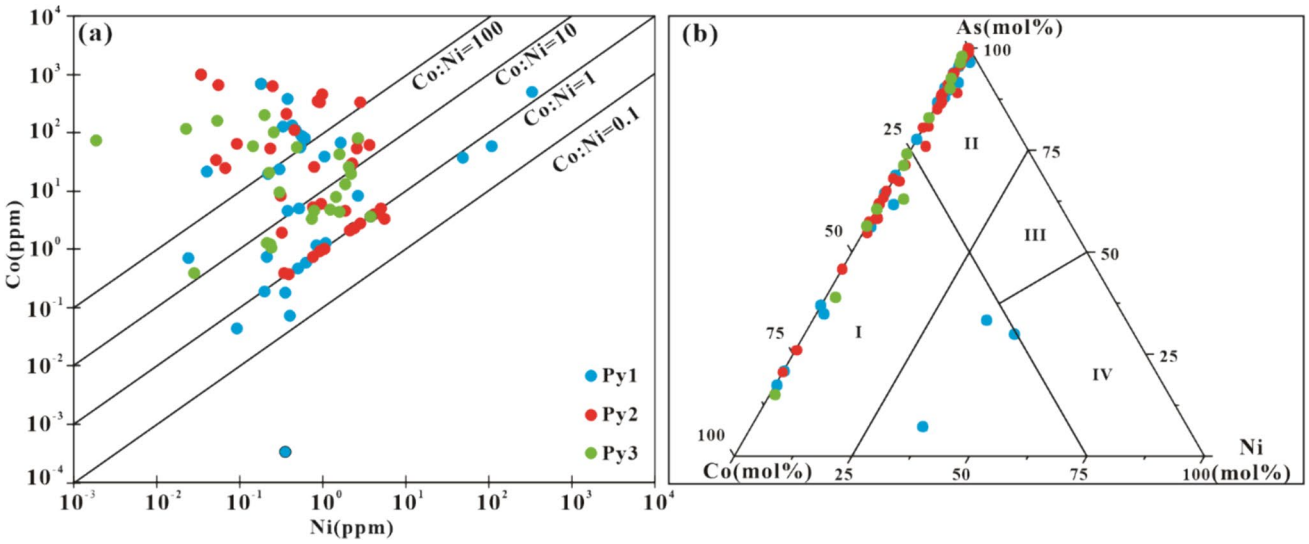

Fig. 14 **a** Co (ppm) versus Ni (ppm) diagrams of pyrite; **b** Co-Ni-As ternary diagram of pyrite [I. magmatic hydrothermal and volcanic hydrothermal types, II. overlap, III. Carlin, IV. metamorphic; the areas of I, II, III and IV are from Yan et al. (2012a, b)]

(Gong et al. 2011; Yan et al. 2012a, b; Yuan et al. 2018; Wang et al. 2021; Cao et al. 2023). Yan et al. (2012a, b) conducted a comparative analysis of the mass fraction ratios of Co, Ni and As in pyrite from various types of gold deposits, categorizing them into magmatic hydrothermal, volcanic hydrothermal, Carlin and metamorphic hydrothermal types. In the Huxu Au-dominated polymetallic deposit, most data points of three-generation pyrites are plotted in magmatic and volcanic hydrothermal regions. Taken together, we contend that the Huxu Au-dominated polymetallic deposit is an epithermal deposit.

Epithermal deposits can be divided into three subtypes: (1) high sulfidation (HS); (2) intermediate sulfidation (IS), (3) low sulfidation (LS) (Taylor 2007; Hedenquist et al. 2000; Song et al., 2018; Wang et al. 2019). Different types of epithermal deposits can be distinguished by ore-forming tectonic background, characteristics of mineralization-related igneous rocks, sulfide content of ores, iron contents of sphalerite, mineral composition, fluid sources and so on (Taylor 2007; Song et al. 2018). For the Huxu Au-dominated polymetallic deposit, it formed in an intracontinental extensional setting in the Late Jurassic to Cretaceous, as evidenced by the red basins and volcanic rocks regionally (Fig. 1a); the primary rocks in the mining area are diorite-porphyry and rhyolite (Fig. 1c); the ore bodies occur predominantly as veins or stockworks (Figs. 1c and 2); the ore contains moderate levels of sulfides (Fig. 3), the sphalerite present is of light color and low-iron (Fig. 3c); carbonate is common in the ores (Figs. 2e and 5i); the ore-forming fluid is a mixture of magmatic water and meteoric water (Fig. 11). These integrated characteristics are consistent with those of the IS epithermal deposit (Song et al. 2018; Wang et al. 2019). The Ag/Au ratios for pyrites from all stages are far greater than 60 (Py1 = 128.1, Py2 = 569.881, Py3 = 398.502); these are identical to IS epithermal deposits in an intracontinental extensional setting (Ag/Au ratios > 60, Wang et al. 2019). In summary, the Huxu Au-dominated polymetallic deposit should be an IS epithermal deposit.

7 Conclusion

This study conducted *in-situ* trace element and S–Pb isotope analysis of pyrite in the Huxu Au-dominated polymetallic deposit. The chemical states of trace elements within the pyrite and the source of both the metals and the ore-forming fluid were discussed. The main conclusions of this study are as follows:

(1) For the pyrite in the Huxu Au-dominated polymetallic deposit, Au primarily exists in the form of visible gold; Pb, Zn and Cu predominantly occur as inclusions of galena, sphalerite and chalcopyrite; Ag, Sb and Bi are primarily associated with galena inclusions.
(2) The ore-forming fluid is a mixture of magmatic and meteoric water, with the ore-forming materials primarily originating from magma.
(3) The fluid boiling and mixing of different fluids are the main reasons for native gold precipitation, while water-rock interaction may be the primary reason for Pb and Zn precipitation.
(4) The Huxu Au-dominated polymetallic deposit belongs to the intermediate sulfidation epithermal deposit.

Acknowledgements We are grateful to the 1st Team of Jiangxi Nonferrous Metals Geological Exploration Bureau and Wei-Wei Chao, Bo Yuan, Jun-Feng Dai, Feng Lai and Jian Zhang from East China University of Technology for their assistance during field geological surveys and the sample collection process. This research was jointly supported by the foundation from Department of Science and Technology of Jiangxi Province (No. 20232BAB213064), National Natural Science Foundation of China (No. 42102088) and foundation from the State Key Laboratory of Nuclear Resources and Environment (2022NRE33).

Author contributions Hongze Gao: writing-original draft, review; Jiajie Chen: article ideation, writing-original draft, review; Chengbiao Leng: review; Yuhui Hu: sample processing, data processing; Huidan Xie: sample processing, data processing; Zenghua Li: review.

Funding This research was jointly supported by the foundation from Department of Science and Technology of Jiangxi Province (No. 20232BAB213064), National Natural Science Foundation of China (No. 42102088) and foundation from the State Key Laboratory of Nuclear Resources and Environment (2022NRE33).

Declarations

Conflict of interest The authors declare that they have no known competing financial interests or personal relationships that could have appeared to influence the work reported in this paper.

References

Bi XW, Hu RZ, Peng JT, Wu KX (2004) REE and HFSE geochemical characteristics of pyrites in Yao'an gold deposit: Tracing ore forming fluid signatures. Bull Min Petrol Geochem 23(1):1–4 (**in Chinese with English abstract**).

Cai YT, Ni P, Shen K, Zhu XT, Huang SJ, Zhang XC, Xu JH (2011) Study on the fluid inclusion from Dongxian copper deposit Jiangxi Province China. Acta Petrol Sin 27(5):1375–1386 (**in Chinese with English abstract**).

Cai YT, Ni P, Wang GG, Pan JY, Zhu XT, Chen H, Ding JY (2016) Fluid inclusion and H-O–S–Pb isotopic evidence for the Dongxiang Manto-type copper deposit, South China. J Geochem Explor 171:71–82. https://doi.org/10.1016/j.gexplo.2016.01.019

Cao GS, Zhang Y, Chen HY (2023) Trace elements in pyrite from orogenic gold deposits implications for metallogenic mechanism.

Acta Petrol Sin 39(8):2330–2346 (**in Chinese with English abstract**). https://doi.org/10.18654/1000-0569/2023.08.06

Chen YJ, Ni P, Fan HR, Pirajno F, Lai Y, Su WC, Zhang H (2007) Diagnostic fluid inclusions of different types hydrothermal gold deposits. Acta Petrol Sin 23(9):2085–2108 (**in Chinese with English abstract**).

Cook N, Spry P, Vokes F (1998) Mineralogy and textural relationships among sulphosalts and related minerals in The Bleikvassli Zn-Pb-(Cu) deposit, Nordland, Norway. Miner Deposita 34:35–56. https://doi.org/10.1007/s001260050184

Fan HR, Li XH, Zuo YB, Chen L, Liu S, Hu FF, Feng K (2018) *In-situ* LA-(MC)-ICPMS and (Nano) SIMS trace elements and sulfur isotope analyses on sulfides and application to confine metallogenic process of ore deposit. Acta Petrol Sin 34(12):3479–3496

Gamarra-Urrunaga JE, Castroviejo R, Bernhardt HJ (2013) Preliminary mineralogy and ore petrology of the intermediate-sulfidation Pallancata deposit, Ayacucho. Peru Canad Mineral 51(1):67–91.

Gong L, Ma G (2011) The characteristic typomorphic composition of pyrite and its indicative meaning to metal deposits. Contrib Geol Miner Resour Res 26(2):162–166 (**in Chinese with English abstract**).

Hedenquist JW, Arribas AN, Gonzalez-Urien E (2000) Exploration for Epithermal Gold Deposits

Hu ZC, Zhang W, Liu YS, Gao S, Li M, Zong KQ, Chen HH, Hu SH (2015) "Wave" signal-smoothing and mercury-removing device for laser ablation quadrupole and multiple collector ICPMS analysis: Application to lead isotope analysis. Anal Chem 87(2):1152–1157.

Hu RZ, Fu SL, Xiao JF (2016) Major scientific problems on low-temperature metallogenesis in South China. Acta Petrol Sin 32(11):3239–3251 (**in Chinese with English abstract**).

Keith M, Smith DJ, Jenkin GRT, Holwell DA, Dye MD (2018) A review of Te and Se systematics in hydrothermal pyrite from precious metal deposits: Insights into ore-forming processes. Ore Geol Rev 96:269–282.

Kouhestani H, Ghaderi M, Chang Z, Zaw K (2015) Constraints on the ore fluids in the Chah Zard breccia-hosted epithermal Au–Ag deposit, Iran: Fluid inclusions and stable isotope studies. Ore Geol Rev 65:512–521.

Large RR, Danyushevsky L, Hollit C, Maslennikov V, Meffre S, Gilbert S, Bull S, Scott R, Emsbo P, Thomas H, Singh B, Foster J (2009) Gold and trace element zonation in pyrite using a laser imaging technique: implications for the timing of gold in Orogenic and Carlin-Style Sediment-Hosted deposits. Econ Geol 104(5):635–668. https://doi.org/10.2113/gsecongeo.104.5.635

Li WX, Li XH (2004) Adakitic granites within the NE Jiangxi Ophiolites, South China geochemical and Nd isotopic evidence. Geol J China Univ 10(2):199–208 (**in Chinese with English abstract**).

Li Z, Li X (2007) Formation of the 1300-km-wide intracontinental orogen and postorogenic magmatic province in Mesozoic South China: A flat-slab subduction model. Geology 35(2):179–182.

Li BL, Zhang H (2010) Some advances in the research of epithermal gold deposit. Acta Mineral Sin 30(1):90–97.

Liu YS, Hu ZC, Gao S, Günther D, Xu J, Gao CG, Chen HH (2008) In situ analysis of major and trace elements of anhydrous minerals by LA-ICP-MS without applying an internal standard. Chem Geol 257(1–2):34–43.

Lu SD, Gao WL, Wang SL, Xiao E, Xu JH, Liu J (2005) Pb isotopic compositions and its singnificance for ore genesis in Zhangshiba Pb-Zn deposit. Jiangxi Mineral Petrol 25(02):64–69 (in Chinese with English abstract). https://doi.org/10.19719/j.cnki.1001-6872.2005.02.011.

Mao JW, Chen MH, Yuan SD, Guo CL (2011) Geological characteristics of the Qinhang (or Shihang) Metallogenic Belt in South China and spatial-temporal distribution regularity of mineral deposits. Acta Geol Sin 85(5):636–658 (**in Chinese with English abstract**).

Mao J, Zheng W, Xie G, Lehmann B, Goldfarb R (2021) Recognition of a Middle-Late Jurassic arc-related porphyry copper belt along the southeast China coast: Geological characteristics and metallogenic implications. Geology 49(5):592–596.

Maslennikov VV, Maslennikova SP, Large RR, Danyushevsky LV (2009) Study of trace element zonation in vent chimneys from the Silurian Yaman-Kasy volcanic-hosted massive sulfide deposit (Southern Urals, Russia) using laser ablation-inductively coupled plasma mass spectrometry (LA-ICPMS). Econ Geol 104(8):1111–1141. https://doi.org/10.2113/gsecongeo.104.8.1111

Mehrabi B, Siani MG (2012) Intermediate sulfidation epithermal Pb-Zn-Cu (±Ag-Au) mineralization at Cheshmeh Hafez deposit, Semnan province Iran. J Geol Soc India 80(4):563–578.

Moncada D, Mutchler S, Nieto A, Reynolds TJ, Rimstidt JD, Bodnar RJ (2012) Mineral textures and fluid inclusion petrography of the epithermal Ag–Au deposits at Guanajuato, Mexico: Application to exploration. J Geochem Explor 114:20–35. https://doi.org/10.1016/j.gexplo.2011.12.001

Ni P, Chi W, Pan JY (2020) An integrated investigation of ore-forming fluid evolution in porphyry and epithermal deposits and their implication on exploration. Earth Sci Front 27(2):060–078.

Ohmoto H (1972) Systematics of sulfur and carbon isotopes in hydrothermal ore deposits. Econ Geol 67(5):551–578. https://doi.org/10.2113/gsecongeo.67.5.551

Ohmoto H (1986) Stable isotope geochemistry of ore deposits. Rev Mineral Geochem 16(1):491–559.

Ouyang XC (2015) Geological and geochemical characteristics and its genesis of the dongxiang copper deposit, Jiangxi Province. China University of Geosciences (Beijing). Published thesis (**in Chinese with English abstract**).

Qin XF (2014) A preliminary framework for the sequence of volcanic-intrusive magma of relation to mineralization in The North Wuyi Yanshanian Area. China University of Geosciences (Beijing) (**in Chinese with English abstract**).

Reich M, Kesler SE, Utsunomiya S, Palenik CS, Chryssoulis SL, Ewing RC (2005) Solubility of gold in arsenian pyrite. Geochim Cosmochim Acta 69(11):2781–2796. https://doi.org/10.1016/j.gca.2005.01.011

Reich M, Deditius A, Chryssoulis S, Li JW, Ma CQ, Parada MA, Barra F, Mittermayr F (2013) Pyrite as a record of hydrothermal fluid evolution in a porphyry copper system: a SIMS/EPMA trace element study. Geochim Cosmochim Acta 104:42–62

Rollinson HR (1993) Using geochemical data: evaluation, presentation, interpretation. Harlow, Essex, England: New York: Longman Scientific & Technical; Copublished in the U.S. with Wiley

Roman N, Reich M, Leisen M, Morata D, Barra F, Deditius AP (2019) Geochemical and micro-textural fingerprints of boiling in pyrite. Geochim Cosmochim Acta 246:60–85. https://doi.org/10.1016/j.gca.2018.11.034

Schaarschmidt A, Haase KM, Klemd R, Manuel K, Voudouris PC, Alfieris D, Strauss H, Wiedenbeck M (2021) Boiling effects on trace element and sulfur isotope compositions of sulfides in shallow-marine hydrothermal systems: evidence from Milos Island Greece. Chem Geol 583:120457. https://doi.org/10.1016/j.chemgeo.2021.120457

Shang LB, Fan WL, Hu RZ, Deng HL (2004) A Thermodynamic study on paragenesis and separation of silver, lead and zincin hydrothermal solutions. Acta Mineral Sin 24(01):81–86 (in Chinese with English abstract). https://doi.org/10.16461/j.cnki.1000-4734.2004.01.013.

Shannon R (1976) Revised effective ionic radii and systematic study of inter atomic distances in halides and chalcogenides. Acta Crystallogr A 32:751–767. https://doi.org/10.1107/s0567739476001551

Shu X, Yang SY, Jiang SY, Ye M (2017) Petrogenesis and geodynamic setting of early cretaceous felsic rocks in the Gan-Hang Belt, Southeast China: constraints from geochronology and geochemistry of the tuffs and trachyandesitic rocks in Shengyuan volcanic Basin. Lithos 284–285:691–708. https://doi.org/10.1016/j.lithos.2017.05.007

Sibson RH (1987) Earthquake rupturing as a mineralizing agent in hydrothermal systems. Geology 15(8):701. https://doi.org/10.1130/0091-7613(1987)15%3c701:ERAAMA%3e2.0.CO;2

Song GX, Qin KZ, Li GM, Wang L (2018) Basic characteristics and research progresses of intermediate sulfidation type epithermal gold poly-metallic deposits, and prospects. Acta Petrol Sin 34(3):748–762.

Su HM, Mao JW, He XR, Lu R (2013) Timing of the formation of the Tianhuashan Basin in Northem Wuyi as constrained by geochronology of volcanic and plutonic rocks. Sci China Earth Sci 56:940–955 (in Chinese with English abstract). https://doi.org/10.1007/s11430-013-4610-9.

Sun WD, Ling MX, Wang FY, Ding X, Hu YH, Zhou JB, Yang XY (2008) Pacific Plate mesozoic geological event in Eastern China. Bull Mineral Petrol Geochem 27(3):218–225 (**in Chinese with English abstract**).

Tauson VL (1999) Gold solubility in the common gold-bearing minerals: experimental evaluation and application to pyrite. Eur J Min 11(6):937–948. https://doi.org/10.1127/ejm/11/6/0937

Taylor HP (1974) The application of oxygen and hydrogen isotope studies to problems of hydrothermal alteration and ore deposition. Econ Geol 69(6):843–883.

Taylor BE (2007) Epithermal gold deposits. Mineral Deposits of Canada: A synthesis of major deposit-types, district metallogeny, the evolution of geological provinces, and exploration methods: Geological Association of Canada, Mineral Deposits Division, Special Publication, 5, 113-139.

Wan L, Zhou T, Dai W, Chang T (2020) Metallogenic geological characteristics and prospecting prediction in the south of Dongxiang Jiangxi Province. World Nonferrous Metal 9:89–90 (**in Chinese with English abstract**).

Wang KY, Lu ZX, Zhang XG (1998) The geological and mineralization feature of Huxu Gold deposit and study on its origin. Golg 5:7–12 (**in Chinese with English abstract**).

Wang GG, Ni P, Wang RC, Zhao KD, Chen H, Ding JY, Zhao C, Cai YT (2013) Geological, fluid inclusion and isotopic studies of the Yinshan Cu–Au–Pb–Zn–Ag deposit, South China: implications for ore genesis and exploration. J Asian Earth Sci 74:343–360. https://doi.org/10.1016/j.jseaes.2012.11.038

Wang L, Qin KZ, Song GX, Li GM (2019) A review of intermediate sulfidation epithermal deposits and subclassification. Ore Geol Rev 107:434–456.

Wang K, Zhai D, Liu J, Wu H (2021) LA-ICP-MS trace element analysis of pyrite from The Dafang gold deposit, South China: implications for ore genesis. Ore Geol Rev 139:104507. https://doi.org/10.1016/j.oregeorev.2021.104507

Yan YT, Li SR, Jia BJ, Zhang N, Yan LN (2012a) Composition typomorphic characteristics and statistic analysis of pyrite in gold deposits of different genetic types. Earth Sci Front 19(4):214–226 (**in Chinese with English abstract**).

Yan JL, Jiang JJ, Zhang J, Zhang J, Wu ZC, Zhu XP (2012b) Metallogenic geological and geochemical characteristics and ore-prospecting potential of Dongxiang volcanic area Jiangxi Province. Geophys Geochem Explor 36(4):534–538.

Yang SY, Jiang SY, Jiang YH, Zhao KD, Fan HH (2011) Geochemical, zircon U-Pb dating and Sr–Nd–Hf isotopic constraints on the age and petrogenesis of an early cretaceous volcanic-intrusive complex at Xiangshan Southeast China. Mineral Petrol 101(1–2):21–48. https://doi.org/10.1007/s00710-010-0136-4

Yang B, Shui YX, Zhao YY, Zhu XY, Wang ZK (2016) H-O-S-Pb isotopic characteristics of the Zhushahong porphyry copper deposit in Dexing, Jiangxi province, and their significance. Acta Geol Sin 90(01):126–138 (**in Chinese with English abstract**).

Yang Q (2015) Age and attribution of volcanic rocks in the Dongxiang Volcanic Basin in The North Wuyi. China University of Geosciences (Beijing) (**in Chinese with English abstract**).

Yilmaz H, Oyman T, Sonmez FN, Arehart GB, Billor Z (2010) Intermediate sulfidation epithermal gold-base metal deposits in Tertiary subaerial volcanic rocks, Sahinli/Tespih Dere (Lapseki/Western Turkey). Ore Geol Rev 37(3–4):236–258.

Yu X, Wu GG, Zhang D, Yan TZ, Di YJ, Wang LW (2006) Cretaceous extension of the Ganhang tectonic belt, Southeastern China: constraints from geochemistry of volcanic rocks. Cretac Res 27(5):663–672. https://doi.org/10.1016/j.cretres.2006.03.008

Yuan MW, Li SR, Li CL, Santosh M, Alam M, Zeng YJ (2018) Geochemical and isotopic composition of auriferous pyrite from the Yongxin gold deposit, central asian Orogenic Belt: implication for ore genesis. Ore Geol Rev 93:255–267. https://doi.org/10.1016/j.oregeorev.2018.01.002

Zartman RE, Doe BR (1981) Plumbotectonics—the model. Tectonophysics 75(1–2):135–162. https://doi.org/10.1016/0040-1951(81)90213-4

Zhang DH (1997a) Overview of research on the ore depositional mechanisms in ore-forming fluid. Geol Sci Technol Inf 16(3):54–59 (**in Chinese with English abstract**).

Zhang DH (1997b) Some new advances in ore-forming fluid geochemistry on boiling and mixing of fluids during the processes of hydrothermal deposits. Adv Earth Sci 12(6):49–55 (**in Chinese with English abstract**).

Zhang W, Hu ZC, Gunther D, Liu YS, Ling WL, Zong KQ, Chen HH, Gao S, Xu L (2016) Direct lead isotope analysis in Hg-rich sulfides by LA-MC-ICP-MS with a gas exchange device and matrix-matched calibration. Anal Chim Acta 948:9–18.

Zhang W, Hu ZC, Liu YS (2020) Iso-compass: New freeware software for isotopic data reduction of LA-MC-ICP-MS. J Anal Spectrom 35(6):1087–1096.

Zhang HY, Zhao QQ, Zhao G, Hong JX, Liu JJ, Zhai DG (2022) In situ LA-ICP-MS trace element analysis of pyrite and its application in study of Au deposit. Min Depos 41(6):1182–1199 (in Chinese with English abstract). https://doi.org/10.16111/j.0258-7106.2022.06.006.

Zhou Q, Jiang YH, Zhao P, Liao SY, Jin GD (2012) Origin of the Dexing Cu-bearing porphyries, SE China: elemental and Sr–Nd–Pb–Hf isotopic constraints. Int Geol Rev 54(5):572–592. https://doi.org/10.1080/00206814.2010.548119

Zhou XJ, Li SQ, Chen LQ (2019) Discussion of metallogenic regularity and prospecting direction of Dongxiang volcanic basin in Jiangxi province. J East China Univ Technol (Nat Sci) 42(1):45–51 (**in Chinese with English abstract**).

Zong KQ, Klemd R, Yuan Y, He ZY, Guo JL, Shi XL, Liu YS, Hu ZC, Zhang ZM (2017) The assembly of Rodinia: the correlation of early neoproterozoic (ca. 900 Ma) high-grade metamorphism and continental arc formation in the Southern Beishan Orogen, Southern Central Asian Orogenic Belt (CAOB). Precambr Res 290:32–48.